Discrete elastica for shape design of gridshells

AUTHOR(S):

Sakai, Yusuke; Ohsaki, Makoto

Submitted to Engineering Structures

Discrete elastica for shape design of gridshells

Yusuke Sakai[1] and Makoto Ohsaki[2]

[1]Department of Architecture and Architectural Engineering, Kyoto University, Kyoto-Daigaku Katsura, Nishikyo, Kyoto 615-8540, Japan, sakai.yusuke.52v@st.kyoto-u.ac.jp

[2]Department of Architecture and Architectural Engineering, Kyoto University, Kyoto-Daigaku Katsura, Nishikyo, Kyoto 615-8540, Japan, ohsaki@archi.kyoto-u.ac.jp

Abstract

This paper presents an approach to designing a gridshell structure, which is constructed connecting beams under bending deformation by hinge joints. The gridshell is modeled as an assembly of piecewise linear curves called 'discrete elastica', which is a discretized form of elastica defined as the shape of buckled beam-column with large deflections. Shape parameters such as span, height at the support, height at the internal joint, and the external moments are assigned to generate various shapes of discrete elastica, which are found by minimizing the total potential energy. It is shown in the numerical examples that a gridshell surface designed using discrete elastica has small interaction forces between the curved beams at joints. Large deformation analysis is carried out for verification of the shape generated using discrete elastica. An optimization approach is presented to further reduce the interaction forces between beams by assigning specified number of 'hinge+slot joints' to allow relative translational displacement at a hinge. Finally, the static structural characteristics of optimal gridshells are investigated.

Keywords: gridshell, discrete elastica, large-deformation analysis, bending-active structures

1. Introduction

Gridshell structure is one of the most efficient roof structures in view of construction period of time and cost [1, 2]. For example, the Mannheim Bundesgartenschau in Germany and the

*A part of this paper has been presented at Annual Symposium of International Association for Shell and Spatial Structures (IASS2017), Hamburg, Germany, 2017.

Downland gridshell in UK are often cited as efficient structures in view of lightweight and mechanically efficient properties. Shape of a gridshell is generated from straight beams that are connected by hinge joints. The beams are first connected on a plane to form a grid with rectangular units. Then forced deformation and external moments are given at the boundary to obtain a curved surface. Note that the term *gridshell* is also used for a single-layer latticed shell with continuous beams in two directions. However, in this paper, we assume that *gridshell* means a *bending-active* structure constructed by bending beams and assembling them into a grid shape.

There are two popular methods for form-finding of a curved surface: namely, inversion method [3,4], dynamic relaxation method [5,6], and force density method [7,8]. The inversion method is based on the simple idea that a curved surface is obtained by inverting a shape of suspended flexible net under self-weight, which is experimentally or numerically obtained. This way, a shape dominated by compression is successfully generated. This method obtains an equilibrium shape of a structure by simulating the damped vibration process with artificial damping parameters. The dynamic relaxation method obtains a self-equilibrium shape by simulating dynamic vibration process to converge to a static equilibrium state using an artificial mass and damping. The force density method is mainly used for finding an equilibrium shape of structure in which axial forces dominate.

If the initial plane grid has square units, then all members between joints have the same length. A curved surface with uniform grid size can be generated by using various existing methods such as compass method [3, 7] and particle-spring method [8]. However, restriction of uniform grid substantially limits the shape of curved surface generated from a plane grid. Furthermore, the interaction forces at joints become very large, if the final shape of surface is not appropriate.

Since the axial forces and bending moments in beams as well as the interaction forces at joints are highly dependent on the shape at self-equilibrium of a bending-active gridshell, it is useful to tune up the shape using an optimization method. However, only a few optimization methods have been presented for design of gridshells. Bouhaya *et al*. [4] optimized the geometrical parameters using genetic algorithm for minimizing the maximum curvature of surface. Ohsaki *et al*. [9] and Matsuo *et al*. [10] presented a method for reducing the interaction forces between beams by placing slots at the joint. They defined the target shape of curved beams as elastica [11-13], which is the shape of a buckled beam-column with large deformation. However, to obtain the target shape, a differential equation needs to be solved with respect to the arc-length parameter [14].

In this paper, we present a method for designing shapes of gridshell structures using discrete elastica model [15, 16], which has been studied in the field of computer science. This model

enables us to generate easily the target shape of curved beams that are in self-equilibrium state with bending moment against forced support displacements. It is verified through large-deformation analysis that the shape of discrete elastica is very close to the shape of continuous elastica. In addition, we show that a curved surface in three-dimensional space with small interaction forces at joints can be generated by connecting several discrete elasticas. The interaction forces at joints are further reduced by placing *hinge+slot joint* that allows relative displacement of nodes of a hinge in the direction of a beam [9]. Optimal locations of hinge+slot joints are found using simulated annealing (SA) [17-19], and static structural behavior of the optimal curved surface is investigated.

2. Shape design of discrete elastica

Elastica is defined as a shape of buckled beam-column under point loads at both ends. Property of the buckled beam was studied by many mathematicians, and Leonhard Euler (1707-1783) studied the properties of the elastica by means of calculus of variations [20]. The deflected equilibrium shape of elastica is obtained by solving a differential equation with respect to the arc-length parameter [14], which may also be solved using a forward difference approach [9].

The shape can be alternatively obtained by minimizing an energy functional. The bending stiffness, curvature, and arc-length parameter of a continuous beam are denoted by EI, κ, and s, respectively. A parameter β (> 0) is given to restrict axial deformation. Then, the penalized strain energy function U is defined as

$$U = \int \left(\frac{1}{2} EI\kappa^2 + \beta \right) \mathrm{d}s \tag{1}$$

which is to be minimized under appropriate boundary and loading conditions. The minimum of U may be found by discretization such as Fourier transformation and other basis function approach. However, it is very difficult to obtain a complex shape composed of multiple curves elastically supported at the ends and the connections of curves, which is used in the following sections to generate the shapes of gridshells.

Meanwhile, discrete elastica is defined as a discretized piecewise linear curve with the same segment length l as shown in Fig. 1. Following the definition in Ref. [15], the model has $N + 2$ nodes denoted by P_i $(i = 0, \ldots, N + 1)$. The number of segments is $N + 1$, and the ith segment connects nodes i and $i + 1$. The deflection angle of segment i from x-axis and the angle between the segments $i - 1$ and i are denoted by Ψ_i and θ_i $(= \Psi_{i-1} - \Psi_i)$, respectively.

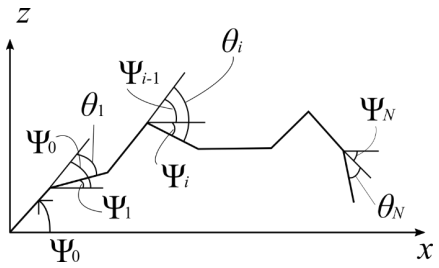

Figure 1: Piecewise linear planar curve with same segment length. Total number of segments is $N+1$ in accordance with Ref. [15].

We assign rotational springs at all nodes representing bending stiffness of members. The stiffness of each rotational spring is derived from the equivalence of the strain energy between the discrete elastica and the continuous elastica with bending stiffness EI. Deformation of a segment of the continuous elastica with a curvature κ is equivalent to deformation of the discrete elastica with the spring rotation $\theta = \kappa l$ assuming uniform curvature in the continuous elastica. Hence, the strain energy S of a rotational spring of the discrete elastica is defined as

$$S = \frac{1}{2} EI\kappa^2 l = \frac{1}{2} EI \left(\frac{\theta}{l} \right)^2 l = \frac{EI}{2l} \theta^2 \tag{2}$$

Thus, stiffness of the rotational spring at each node is obtained as EI/l.

The external moments M_0 and M_{N+1} are given at the both ends to generate various shapes. It is possible to assign forced rotations at both ends instead of applying external moments. However, we apply moments for ensuring equal loading conditions for discrete and continuous elasticas in verification process. The objective function is the total potential energy consisting of the discretized form of strain energy and the external work corresponding to the external moments. We assign constraints on the span L and the height difference H between the left support P_0 and the right support P_{N+1}. The optimization problem for minimizing the penalized total potential energy Π with respect to the N+2 variables $\boldsymbol{\Psi} = (\Psi_0, \ldots, \Psi_N)$ and l is formulated as

$$\min_{\boldsymbol{\Psi}, l} \quad \Pi(\boldsymbol{\Psi}, l) = \sum_{i=1}^{N} \left[\frac{EI}{2l} (\Psi_i - \Psi_{i-1})^2 + \beta l \right] - M_0 \Psi_0 - M_{N+1} \Psi_N \tag{3a}$$

$$\text{subject to} \quad \sum_{i=0}^{N} l \cos \Psi_i = L \tag{3b}$$

$$\sum_{i=0}^{N} l \sin \Psi_i = H \tag{3c}$$

Let λ_1 and λ_2 denote the Lagrange multipliers for the constraints (3b) and (3c), respectively. The Lagrangian is formulated as

$$\mathcal{L}\left(\boldsymbol{\Psi}, l; \lambda_1, \lambda_2\right) = \Pi + \lambda_1\left(\sum_{i=0}^{N} l\cos\Psi_i - L\right) + \lambda_2\left(\sum_{i=0}^{N} l\sin\Psi_i - H\right) \tag{4}$$

Taking derivatives of $\mathcal{L}\left(\boldsymbol{\Psi}, l; \lambda_1, \lambda_2\right)$ with respect to the $N+2$ variables $\boldsymbol{\Psi}$ and l, we have the following stationary conditions:

$$\frac{EI\left(-\Psi_{i-1} + 2\Psi_i - \Psi_{i+1}\right)}{l^2} - \lambda_1\sin\Psi_i + \lambda_2\cos\Psi_i = 0, \quad \left(i = 1,\ldots,N-1\right) \tag{5}$$

$$\frac{1}{l}\left[\frac{EI\left(\Psi_1 - \Psi_0\right)}{l} - M_0\right] - \lambda_1\sin\Psi_0 + \lambda_2\cos\Psi_0 = 0 \tag{6}$$

$$\frac{1}{l}\left[\frac{EI\left(\Psi_N - \Psi_{N-1}\right)}{l} - M_{N+1}\right] - \lambda_1\sin\Psi_N + \lambda_2\cos\Psi_N = 0 \tag{7}$$

$$-\sum_{i=1}^{N}\frac{EI}{2}\left(\frac{\Psi_i - \Psi_{i-1}}{l}\right)^2 + \beta + \lambda_1\sum_{i=0}^{N}\cos\Psi_i + \lambda_2\sum_{i=0}^{N}\sin\Psi_i = 0 \tag{8}$$

It is easily confirmed using the relation $M_i = (EI/l)\theta_i = (EI/l)(\Psi_i - \Psi_{i-1})$ that Eqs. (5), (6), and (7) are the equilibrium equations of moment at node $i\,(=1,\ldots,N-1)$, 0, and N, respectively, if the Lagrange multipliers λ_1 and λ_2 represent the support reaction forces in horizontal and vertical directions, respectively, as shown in Fig. 2. Eq. (8) defines the relation between $\boldsymbol{\Psi}$ and l. Since β is the penalty parameter for the total length, a larger value of β leads to a shorter segments. In the following examples, we set $\beta = 1000$ [N], which reduces the rise slightly from the case of $\beta = 0$.

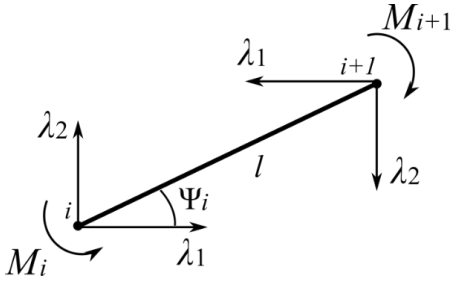

Figure 2: Forces acting on segment i. Lagrange multipliers represent the reaction forces in vertical and horizontal directions.

3. Comparison between discrete and continuous elasticas

In this section, the shape of discrete elastica obtained by solving problem (3) is compared with the shape of continuous elastica obtained by large-deformation analysis. Sequential quadratic programming available in the library SNOPT Ver. 7 [21] is used for energy minimization of the discrete elastica, where the sensitivity coefficients are approximated by finite difference approach.

Abaqus Ver. 6.16 [22] is used for large-deformation analysis of continuous beams. Forced displacements and external moments are given, as shown in Fig. 3, at the both ends of a straight beam on a plane. Length of the beam is equal to the total length of the discrete elastica obtained by solving the optimization problem (3). The beam has a pin support at the left end, and a forced displacement is given at the right end assuming the translational displacements are constrained by a rigid column. In addition, the external moments with the same values as discrete elastica are applied at the both supports. Material of the beam is elastic glass fiber reinforced polymer (GFRP) with Young's modulus 25 GPa and Poisson's ratio 0.221. The beam has a pipe section with radius 0.05 m and thickness 0.005 m.

The loading (path) parameter t is increased from 0.0 to 2.0. Upward virtual load equivalent to self-weight is applied to all members from $t = 0.0$ to 1.0 to prevent numerical difficulty due to out-of-plane bifurcation buckling at the initial plane state. In the period $1.0 \leq t \leq 2.0$, the virtual load is linearly removed, while the forced displacements and external moments are linearly increased at the both ends of the beam. The process of generating the curved shape of continuous elastica is illustrated in Fig. 3.

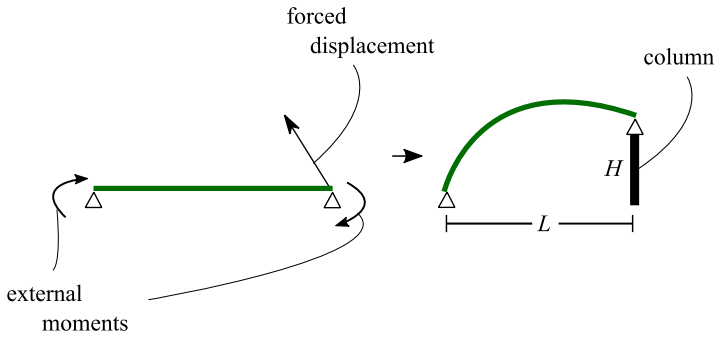

Figure 3: Initial and deformed shapes of a continuous elastica.

Figures 4(a) and (b) show the results of large-deformation analysis of two curves with the parameter values in Table 1. The beam is discretized into 20 segments for the discrete elastica, and 20 beam elements for the continuous elastic. The shapes of continuous elasticas for $\beta = 1000$ [N] and $\beta = 0$ are shown with red and blue lines, respectively, in Figs. 4(a) and (b).

Because the shapes of discrete and continuous elasticas are very close without any visible difference, the shapes of discrete elastica are indicated only by cross-mark and triangle at nodes for $\beta = 1000$ [N] and $\beta = 0$, respectively. As seen from the figure, a larger value of β leads to a smaller height of a curve. The total lengths of discrete elasticas of Curves 1 and 2 are 11.845 m and 21.516 m, respectively. The total contraction of the continuous elasticas of Curves 1 and 2 are 0.1192 mm and 0.4010 mm, respectively, which are very small. Table 2 shows the reaction forces of discrete and continuous elasticas derived from optimization and large-deformation analysis, respectively. The slight difference between the reaction forces of discrete and continuous elasticas is due to discretization of the curve.

Table 1: Parameter values of Curves 1 and 2.

	Curve 1	Curve 2
M_0 [kNm]	−8.00	−10.00
M_{N+1} [kNm]	8.00	−10.00
L [m]	10.0	20.0
H [m]	0.0	4.0
EI [kNm^2]	42.202	42.202

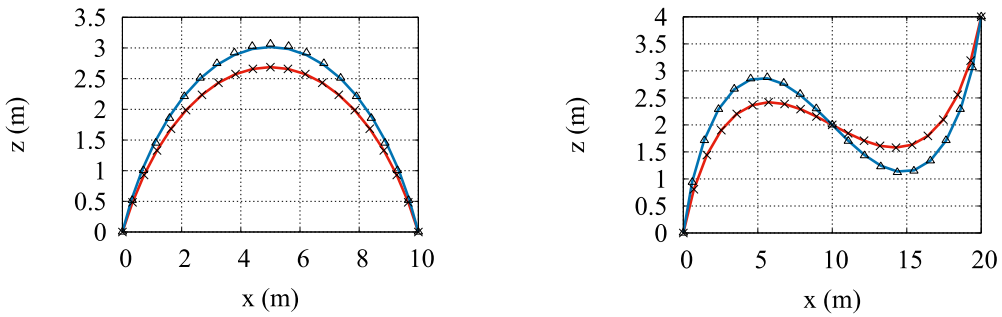

(a) (b)

Figure 4: Shapes of Curves 1 and 2; blue line: continuous elastica ($\beta = 0$), red line: continuous elastica ($\beta = 1000$ [N]), triangle: discrete elastica ($\beta = 0$), circle: discrete elastica ($\beta = 1000$ [N]); (a) Curve 1, (b) Curve 2.

Table 2: Reaction forces in vertical and horizontal directions of discrete and continuous elasticas.

	Curve 1		Curve 2	
	Discrete elastica	Continuous elastica	Discrete elastica	Continuous elastica
λ_1[kN] (Horizontal dir.)	0.4342	0.4449	0.8940	0.9140
λ_2[kN] (Vertical dir.)	0.0000	0.0002	0.8212	0.8171

4. Shape design by connecting multiple curves of discrete elastica

We connect multiple curves of discrete elastica sequentially in the same plane to generate a more complex shape. The process is described, for simplicity, for the case where two curves with $2N+3$ nodes in total are connected. The first and second curves consist of nodes $P_0, \ldots, P_{N+1}$ and $P_{N+1}, \ldots, P_{2(N+1)}$, respectively. We assign a rotational spring at the internal boundary node P_{N+1} between the two curves, and pin supports at both ends P_0 and $P_{2(N+1)}$. The rotational spring at node P_{N+1} has very small stiffness $\hat{\alpha}$. This spring enables moment to be transmitted between the two curves. The span length is L for both curves, and the heights at the internal boundary and the right support are H_1 and H_2, respectively. The optimization problem to find the shape of sequentially connected two discrete elasticas is formulated as

$$\min_{\boldsymbol{\Psi},l} \quad \Pi(\boldsymbol{\Psi},l)=\sum_{i=1}^{N}\left[\frac{EI}{2l}\left(\Psi_i-\Psi_{i-1}\right)^2+\beta l\right]+\sum_{i=N+2}^{2N+1}\left[\frac{EI}{2l}\left(\Psi_i-\Psi_{i-1}\right)^2+\beta l\right] +\frac{\hat{\alpha}}{2}\left(\Psi_{N+1}-\Psi_N\right)^2+\beta l-M_0\Psi_0-M_{2(N+1)}\Psi_{2N+1} \tag{9a}$$

$$\text{subject to} \quad \sum_{i=0}^{N} l\cos\Psi_i = L \tag{9b}$$

$$\sum_{i=0}^{N} l\sin\Psi_i = H_1 \tag{9c}$$

$$\sum_{i=N+1}^{2N+1} l\cos\Psi_i = L \tag{9d}$$

$$\sum_{i=N+1}^{2N+1} l\sin\Psi_i = -H_1+H_2 \tag{9e}$$

Let λ_1, λ_2, λ_3, and λ_4 denote the Lagrange multipliers for the constraints (9b), (9c), (9d), and (9e), respectively. These Lagrange multipliers at the optimal solution are reaction forces at both ends P_0 and $P_{2(N+1)}$ of the connected curves. We solve the optimization problem with parameter values in Table 3 to design shapes of connected discrete elasticas, and to compare the shapes with those of continuous elasticas obtained by large-deformation analysis as described in Sec. 3. The total lengths of Curves 3 and 4 are 21.049 m and 42.322 m , respectively. The left and right ends of the connected discrete elastica are pin supported. The internal connection is also pin supported after deformation assuming that the column has sufficiently large vertical and lateral stiffness.

Table 3: Parameter values of Curves 3 and 4.

	Curve 3	Curve 4
M_0 [kNm]	−8.00	−7.50
$M_{2(N+1)}$ [kNm]	8.00	7.50
L [m]	10.0	20.0
H_1 [m]	2.0	2.0
H_2 [m]	0.0	5.0
EI[kNm^2]	42.202	42.202
$\hat{\alpha}$[Nm]	3.801×10^{-3}	1.890×10^{-3}

The deformation process of a connected continuous elastica is illustrated in Fig. 5. Figures 6(a) and (b) show the results of large-deformation analysis, where the blue lines are the continuous elasticas. Because the shapes of discrete and continuous elasticas are very close without any visible difference, the shapes of discrete elastica are indicated only by circle at nodes. Table 4 shows the reaction forces of discrete and continuous elasticas derived from optimization and large-deformation analysis, which are very close.

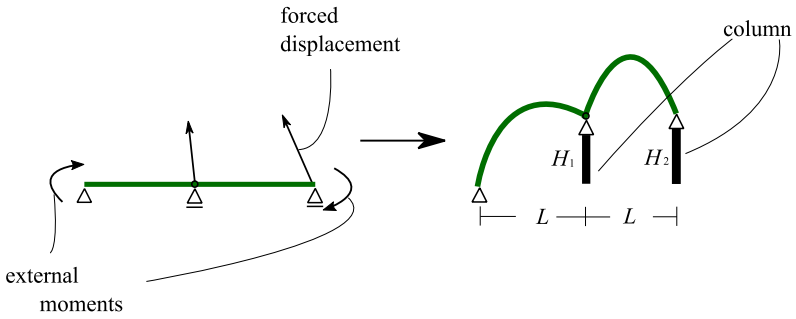

Figure 5: Initial and deformed shapes of a connected continuous elastica.

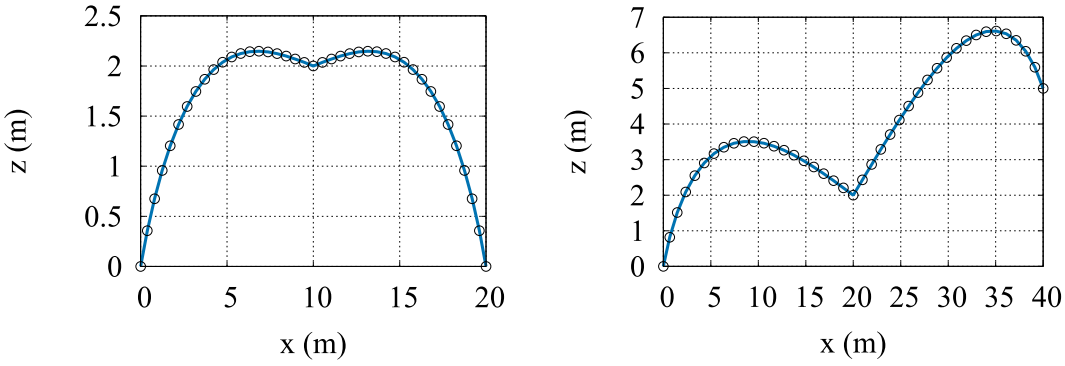

(a) (b)

Figure 6: Shapes of Curves 3 and 4; blue line: continuous elastica, circle: discrete elastica; (a) Curve 3, (b) Curve 4.

Table 4: Reaction forces in vertical and horizontal directions of discrete and continuous elasticas.

	Curve 3		Curve 4	
	Discrete elastica	Continuous elastica	Discrete elastica	Continuous elastica
λ_1[kN] (Horizontal dir.)	0.9540	0.9667	0.8923	0.8992
λ_2[kN] (Vertical dir.)	0.6092	0.6066	0.2858	0.2848
λ_3[kN] (Horizontal dir.)	0.9540	0.9667	0.9209	0.9281
λ_4[kN] (Vertical dir.)	0.6092	0.6066	0.5131	0.5142

5. Generating target surfaces using discrete elastica

In this section, we generate three types of target surface of gridshell using discrete elastica, and compare them with those generated by large-deformation analysis. Surface 1 has different heights in the primary members. Surface 2 has pairs of sequentially connected members. Surface 3 has a rhombus plane that is different from the shapes of Surfaces 1 and 2. All members are connected at joints allowing rotation only along the normal axis of the surface, except the joints of primal members of Surface 2, which allow only rotation along the normal axis of the plane containing the primal members.

The beams are hollow cylinders. The radius and thickness are 0.08 m and 0.008 m, respectively, for the primary beams modeled as elastica. The secondary beams connecting the primary beams have small radius 0.0475 m and thickness 0.003 m to reduce the interaction forces between beams at nodes. Young's modulus, Poisson's ratio, and yield stress are 25 GPa, 0.221, and 200 MPa, respectively.

Surface 1:

Surface 1 is composed of four elasticas along the boundary and two in the diagonal planes of symmetry. Figure 7(a) shows the target surface generated by connecting six primary beams modeled as discrete elastica. The plan of surface is a 10 × 10 (m) square. The parameter values are listed in Table 5. Curve A represents the curves along the exterior boundary, whose height difference is 2 m. Curves B and C represent the curves in the diagonal planes of symmetry, which intersect with each other at the center. The both ends of Curve B are on the ground and the both ends of Curve C are connected to columns with the height 2 m. Primary curves A, B, and C are connected with secondary beams with small section.

Table 5: Parameter values of Curves A, B, and C of Surface 1.

	Curve A	Curve B	Curve C
M_0 [kNm]	−35.343	−30.000	−21.151
M_{N+1} [kNm]	35.343	30.000	21.151
L [m]	10.0	14.142	14.142
H [m]	2.0	0.0	0.0
EI [kNm^2]	276.581	276.581	276.581

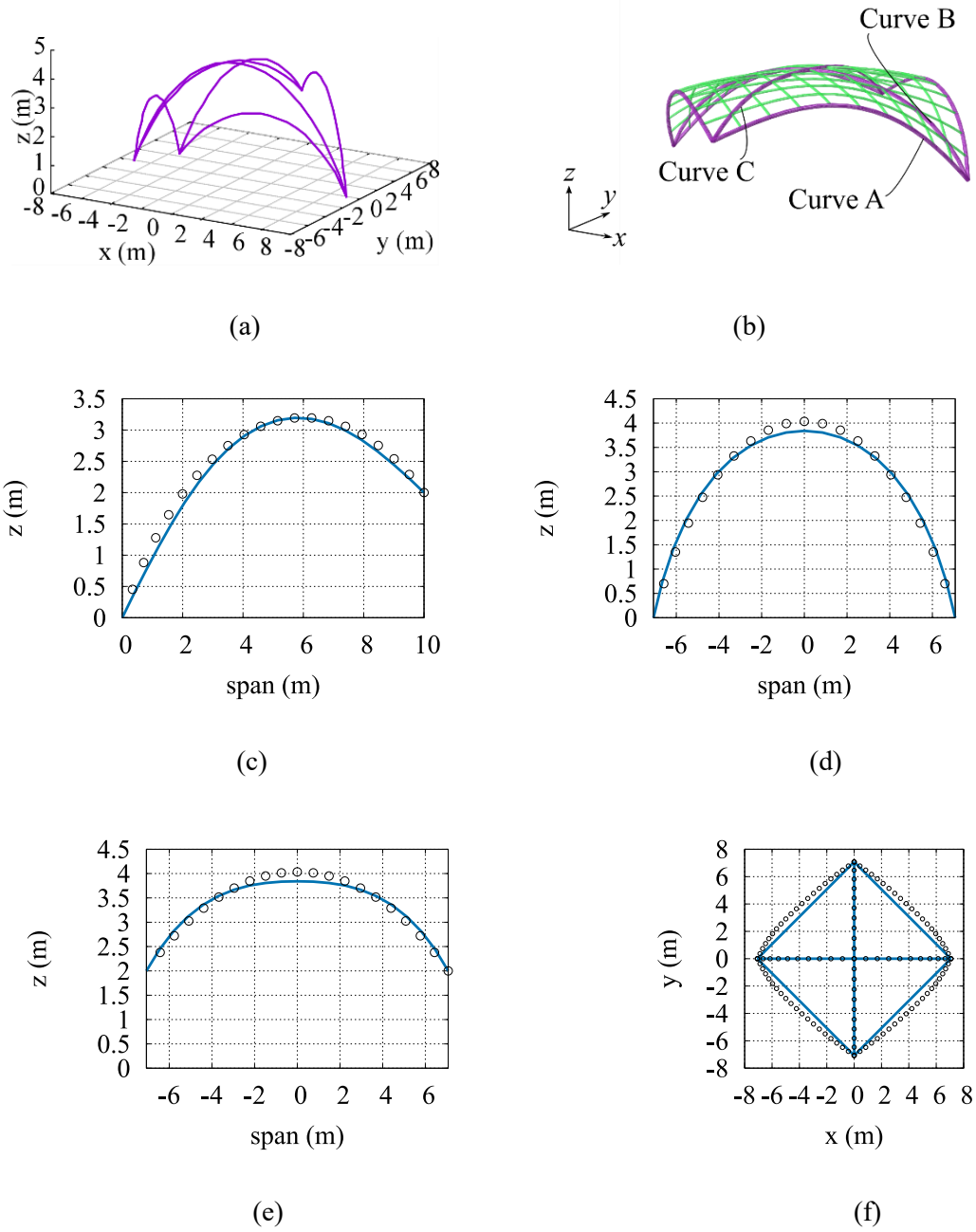

Figure 7: Comparison between the target shape and the shape obtained by large-deformation analysis of Surface 1; blue line: continuous elastica, circle: discrete elastica, (a) target shape of primary beams modeled by discrete elastica, (b) shape of gridshell obtained by large-deformation analysis, (c) Curve A, (d) Curve B, (e) Curve C, (f) plan view.

Figure 7(b) shows the shape of gridshell generated by large-deformation analysis assigning boundary conditions and external moments. Figures 7(c)-(e) show the shapes of discrete elastica and continuous beam of Curves A, B, and C, respectively. The circles and blue lines are the shapes of discrete elastica and continuous beam, respectively, divided into 20 segments and elements. As seen from the figures, the shapes of discrete and continuous elasticas are very close. Note that all member stresses are confirmed to be smaller than the yield stress. It is seen from Fig. 7(f) that the continuous elasticas have out-of-plane deformation with torsion; therefore, they are deflected in horizontal directions.

Surface 2:

We generate Surface 2 parallelly locating eight curves in y-direction as shown in Fig. 8(a). Each curve consists of two elasticas connected at the internal joint supported by a rigid column. The both ends of the connected curve are located on the ground. Surface 2 is symmetric with respect to xz- and yz-planes. Each secondary beam connecting seven primary beams is divided into two parts that are pin-jointed to the primary beam in *yz*-plane.

The parameter values of four types of curves are listed in Table 6. Curves A, B, C, and D are located at $x = 0,\ \pm 2,\ \pm 4$, and ± 6 (m), respectively. The total lengths of Curves A, B, C, and D are 21.453, 25.453, 29.453, and 33.453 (m), respectively. The surface obtained by large-deformation analysis is shown in Fig. 8(b).

Figures 8(c)-(f) show the shapes of Curves A, B, C, and D, respectively. The circles and blue lines are the shapes of discrete and continuous elasticas, respectively, divided into 40 segments and elements. As seen from the figures, the difference between the shapes of discrete and continuous elasticas becomes larger as the distance of the curve from *yz*-plane increases. This is due to large restriction by secondary beams. It has been confirmed that all member stresses obtained by large-deformation analysis are smaller than the yield stress.

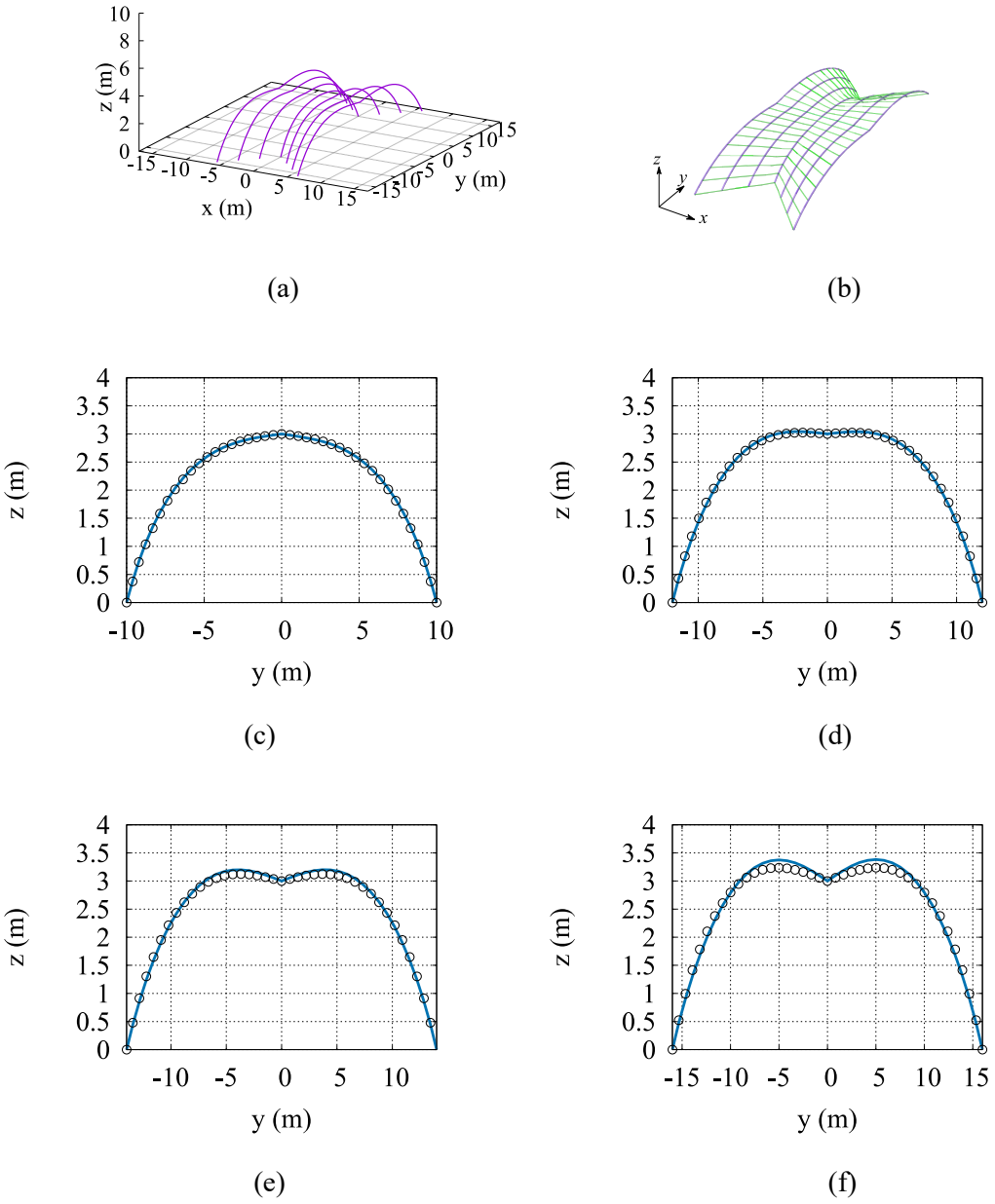

Figure 8: Comparison between the target shape and the shape obtained by large-deformation analysis of Surface 2; blue line: continuous elastica, circle: discrete elastica, (a) target shape of primary beams modeled by discrete elastica, (b) shape of gridshell obtained by large-deformation analysis, (c) Curve A $(x = \pm 1)$, (d) Curve B $(x = \pm 3)$, (e) Curve C $(x = \pm 5)$, (f) Curve D $(x = \pm 7)$.

Table 6: Parameter values of Curves A, B, C, and D of Surface 2.

	Curve A	Curve B	Curve C	Curve D
x-coordinate	± 1	± 3	± 5	± 7
M_0 [kNm]	–40.000	–35.047	–30.670	–27.080
$M_{2(N+1)}$ [kNm]	40.000	35.047	30.670	27.080
L [m]	20.0	24.0	28.0	32.0
H_1 [m]	3.0	3.0	3.0	3.0
H_2 [m]	0.0	0.0	0.0	0.0
EI [kNm^2]	276.581	276.581	276.581	276.581

Surface 3:

Surface 3 is composed of the three same elasticas, called Curve A, along the boundary as shown in Fig. 9(a). The plan of surface is an equilateral triangle with side length 10 m. The both ends of these elasticas are located on the ground, and the parameter values are listed in Table 7. The surface obtained by large-deformation analysis is shown in Fig. 9(b).

Figures 9(c) and (d) show the elevation and plan view of Curve A, respectively. The circlesand blue lines are the discrete and continuous elasticas divided into 20 segments and elements, respectively. As seen from the figures, the shapes of discrete and continuous elasticas are very close, although plan views are a little different, because the size of the plan of undeformed state is larger than that of the curved surface, and the contraction of the plane is restricted by the secondary beams. It has been confirmed that all member stresses obtained by large-deformation analysis are smaller than the yield stress.

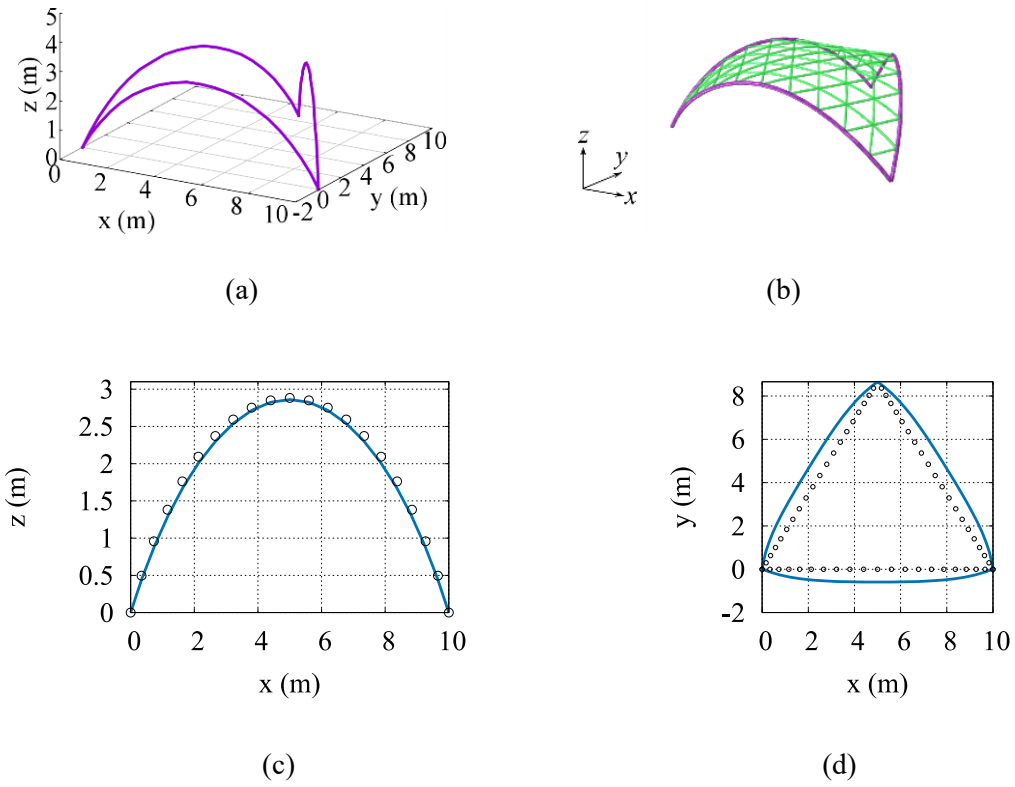

Figure 9: Comparison between the target shape and the shape obtained by large-deformation analysis of Surface 3; blue line: continuous elastica, circle: discrete elastica,
(a) target shape of primary beams modeled by discrete elastica, (b) shape of gridshell obtained by large-deformation analysis, (c) elevation of Curve A, (d) plan view.

Table 7: Parameter values of Curve A of Surface 3.

	Curve A
M_0 [kNm]	–40.000
M_{N+1} [kNm]	40.000
L [m]	10.0
H [m]	0.0
EI [kNm^2]	276.581

6. Optimal locations of hinge+slot joints for reducing interaction forces at joints

It is expected that the gridshell composed of discrete elastica model has small interaction forces at hinge joints, because each beam is in self-equilibrium state under forced displacement at supports. However, interaction force still exists due to constraints by the secondary members. In this section, to further reduce the interaction forces, we assign *hinge+slot joints*, as shown in Fig. 10, at selected nodes to allow relative displacement at node in the direction of a beam. Obviously,

the interaction forces can be drastically reduced by placing hinge+slot joints at all nodes. However, we should find the optimal locations of hinge+slot joints in view of construction cost. Therefore, a combinatorial optimization problem is to be solved.

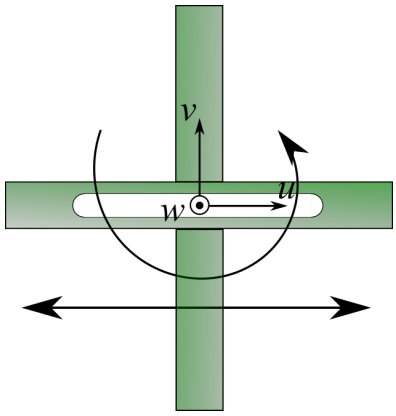

Figure 10: Illustration of hinge+slot joint.

The local coordinates of a bolt are defined such that u-direction is the axial direction of beam, w-direction is the axial direction of the bolt that is placed in one of the principal axis of beam, and v-direction is the remaining principal axis of beam. Let C_{su}^i, C_{sv}^i, and C_w^i denote the two transverse shear forces and the axial force, respectively, of the bolt at the ith node. The allowable shear and axial stresses are denoted by f_s and f_t, respectively. The unconstrained optimization problem is formulated as follows for minimizing the objective function, which is the sum of the stress ratios [23] of interaction forces at all nodes:

$$\min. \quad \sum_{i=1}^{J} \left(\frac{\sqrt{\left(C_{su}^i\right)^2 + \left(C_{sv}^i\right)^2}}{f_s} + \frac{\left|C_w^i\right|}{f_t} \right) \tag{10}$$

where J is the total number of candidate locations of hinge+slot joints. Stress ratios of two connections located at the same coordinates at the initial plane state are defined as the sum of these stress ratios.

Table 8 shows the properties of joints and bolts used for Surfaces 1-3, where f_s and f_t are specified based on the strength classification of Japanese building code [23]. The hinge+slot joints can move along the beams in the range of ± 0.05 m. The optimization problem (10) hence perturbs the target shape of gridshell surface obtained by solving problem (9) for primary beams, which are then connected by secondary beams. SA [17] is used for solving the combinatorial problem; see Appendix for details. In the following examples, the number of steps is 100, the

number of neighborhood solutions is 10, the initial temperature is 1.0, and the temperature reduction ratio η is 0.96. The scaling parameter α is assigned so that the probability of acceptance of a solution at the initial step is 0.5 for 10 % increase of the objective function. It has been confirmed that the solutions obtained by SA do not have strong dependence on the parameters such as η, because the problem considered here is rather simple. The performance of SA has also been confirmed in a small problem by comparing the results with those obtained by enumeration.

Table 8: Properties of joints and bolts.

Surface	Number of joints	Number of candidate locations	Nominal bolt diameter	Effective sectional area (mm^2)	f_s (MPa)	f_t (MPa)
1	143	52	M27	459	74.2	129
2	147	36	M24	353	40.8	70.6
3	129	30	M30	561	64.8	112

Surface 1

An optimal solution is found in one of the quarter parts of the surface utilizing symmetry conditions. Six hinge+slot joints are assigned selectively at the 13 candidate locations; therefore, the number of combinations is ${}_{13}C_6 = 1716$. The filled circle in Figure 11 shows the optimal locations of hinge+slot joints. The candidate locations without assignment of hinge+slot joints are shown with blank circle. Note that only nodes on the primary beams are selected as candidate locations. It is seen from this result that hinge+slot joints tend to be located on the either end of Curve A and the overall Curves B and C.

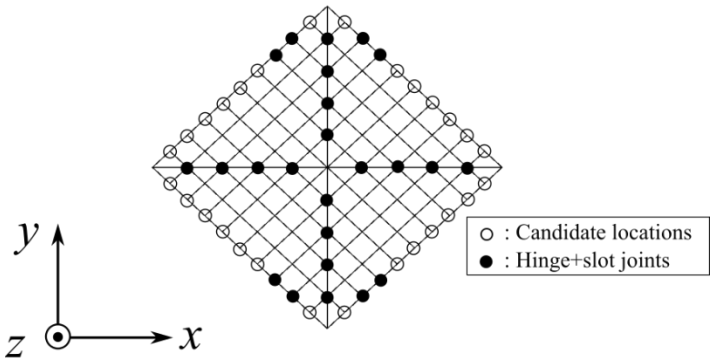

Figure 11: Optimal locations of hinge+slot joints (filled circle) and candidate locations (blank circle) of Surface 1.

Table 9 shows the mean and maximum absolute values of the interaction forces at joints, where 'All hinge' is the case without hinge+slot joints, and 'All hinge+slot' is the case with hinge+slot joints at all 13 candidate locations. Note that the forces are evaluated at all joints including those between secondary beams. It is seen from the table that the maximum values of shear forces C_u and C_v are successfully reduced by optimization to almost the same level as 'All hinge+slot', although the mean values of C_w became larger than the case of 'All hinge'. Table 9 also shows the mean and maximum values of the stress ratio, which have been reduced even to the levels smaller than the case of 'All hinge+slot'. Table 10 shows the mean and maximum quadratic norms of the error between the target shape of the discrete elastica and the shape of corresponding primary beam of the optimal solution. As seen from the table, the error in Curves A, B, and C for 'All hinge' are almost the same as those of the optimal solution. Therefore, using a limited number of hinge+slot joints, the interaction forces can be reduced while maintaining the shape close to the target shape.

Table 9: Mean and maximum absolute values of interaction forces, and mean and maximum values of stress ratio of Surface 1.

			All hinge	All hinge+slot	Optimal
Interaction force	Mean	C_u (kN)	3.9033	2.0917	2.8349
		C_v (kN)	3.5360	2.7460	2.3262
		C_w (kN)	2.7284	3.1273	3.1613
	Max.	C_u (kN)	59.245	33.536	33.532
		C_v (kN)	50.164	25.653	26.425
		C_w (kN)	15.808	16.580	16.933
Stress ratio	Mean	-	0.1368	0.0803	0.0552
	Max.	-	0.9210	0.5557	0.4549

Table 10: Norm of error between target shapes and continuous beams of Surface 1.

		All hinge	All hinge+slot	Optimal
Curve A ($y \geq 0$)	x-dir.	0.2783	0.2764	0.2738
	y-dir.	0.3117	0.3021	0.3020
	z-dir.	0.0783	0.0677	0.0694
Curve A ($y < 0$)	x-dir.	0.2783	0.2764	0.2739
	y-dir.	0.3117	0.3021	0.3021
	z-dir.	0.0783	0.0677	0.0694
Curve B (in xz-plane)	x-dir.	0.0610	0.0661	0.0669
	y-dir.	0.0000	0.0000	0.0002
	z-dir.	0.0976	0.1072	0.1090
Curve C (in yz-plane)	x-dir.	0.0000	0.0000	0.0002
	y-dir.	0.0305	0.0329	0.0333
	z-dir.	0.0993	0.1090	0.1108

Surface 2:

An optimal solution is found in A and B parts in Figure 12 of the surface utilizing symmetry conditions. Hinge+slot joints are assigned at five of the 12 candidate locations; i.e., the number of combinations is ${}_{12}C_5 = 792$. The filled circle in Figure 12 shows the optimal locations of hinge+slot joints. The candidate locations without assignment of hinge+slot joints are also shown in blank circle. As seen from the figure, hinge+slot joints tend to be located close to the both ends of Curves A and B.

Table 11 shows the mean and maximum absolute values of the interaction forces at joints, where 'All hinge+slot' is the case with hinge+slot joints at all 12 candidate locations. It is seen from the table that all components of the maximum interaction forces are successfully reduced by optimization to almost the same level as 'All hinge+slot', although the mean values became larger than the case of 'All hinge'. Table 11 also shows the mean and maximum values of the stress ratio, which are successfully reduced by optimization even to the levels smaller than the case of 'All hinge+slot'. Table 12 shows the mean and maximum norms of the error between the target shape and optimal shape, which has the same property observed for Surface 1. Therefore, using a limited number of hinge+slot joints, the interaction forces can be reduced while maintaining the shape close to the target shape also for Surface 2.

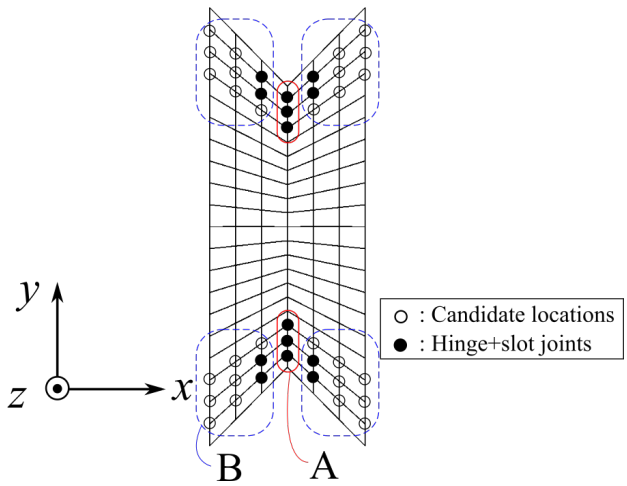

Figure 12: Optimal locations of five hinge+slot joints (filled circle) and candidate locations (blank circle) of Surface 2.

Table 11: Mean and maximum absolute values of interaction forces, and mean and maximum values of stress ratio of Surface 2.

			All hinge	All hinge+slot	Optimal
Interaction force	Mean	C_u (kN)	0.7599	0.7818	0.9203
		C_v (kN)	1.1928	0.7438	0.6836
		C_w (kN)	3.3336	3.0920	3.1413
	Max.	C_u (kN)	16.471	8.1830	6.0700
		C_v (kN)	11.853	9.0790	6.8410
		C_w (kN)	30.995	17.325	20.503
Stress ratio	Mean	-	0.0863	0.0752	0.0772
	Max.	-	0.8427	0.4093	0.3742

Table 12: Norm of error between target shapes and continuous beams of Surface 2.

		All hinge	All hinge+slot	Optimal
Curve A ($x = 0$)	x-dir.	0.0006	0.0005	0.0006
	y-dir.	0.0062	0.0052	0.0051
	z-dir.	0.0104	0.0141	0.0013
Curve B ($x = \pm 2$)	x-dir.	0.0153	0.0111	0.0108
	y-dir.	0.0169	0.0109	0.0109
	z-dir.	0.0188	0.0192	0.0189
Curve C ($x = \pm 4$)	x-dir.	0.0264	0.0193	0.0210
	y-dir.	0.0160	0.0136	0.0147
	z-dir.	0.0474	0.0431	0.0450
Curve D ($x = \pm 6$)	x-dir.	0.0258	0.0223	0.0268
	y-dir.	0.0286	0.0267	0.0273
	z-dir.	0.0853	0.0819	0.0826

Surface 3:

An optimal solution is found in one of the 1/6 parts of the surface utilizing symmetry conditions. Three hinge+slot joints are assigned selectively at the five candidate locations. The number of combinations is ${}_5C_3 = 10$, which is very small; therefore, we enumerated all combinations without using SA. Figure 15 shows the candidate locations and the optimal locations of hinge+slot joints. Here, connections between secondary beams are also selected as candidate locations, because the number of joints on the primary beam is very small. It is seen from Fig. 15 that hinge+slot joints tend to be located around the center of the primary beams as well as the joints between secondary beams.

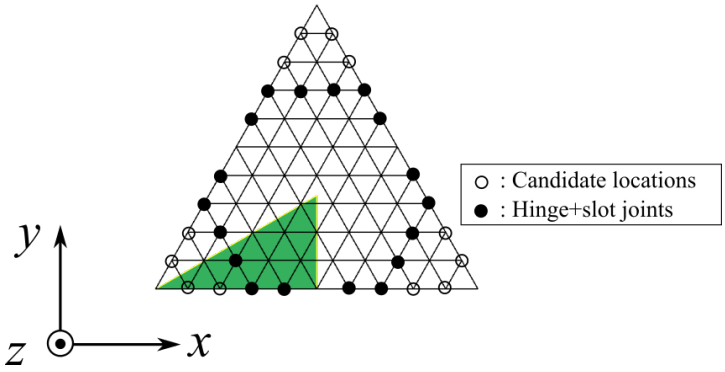

Figure 15: Optimal locations of three hinge+slot joints (filled circle) and candidate locations (blank circle) of Surface 3.

Table 13: Mean and maximum absolute values of interaction forces, and mean and maximum values of stress ratio of Surface 3.

			All hinge	All hinge+slot	Optimal
Interaction force	Mean	C_u (kN)	8.9796	4.8243	4.4739
		C_v (kN)	5.7858	3.6353	3.8224
		C_w (kN)	2.5047	1.6291	2.0673
	Max.	C_u (kN)	36.014	26.274	31.107
		C_v (kN)	31.277	22.827	27.681
		C_w (kN)	10.315	8.4710	8.6980
Stress ratio	Mean	-	0.2128	0.1214	0.1214
	Max.	-	0.6460	0.4339	0.4858

Table 13 shows the mean and maximum absolute values of the interaction forces at joints, where ‘All hinge+slot’ is the case with hinge+slot joints at all five candidate locations. It is seen from the table that all components of the mean and maximum interaction forces are successfully reduced to almost the same level as ‘All hinge+slot’. Table 13 also shows the mean and maximum values of the stress ratio, which are successfully reduced by optimization. Table 14 shows the mean and maximum norms of the error between the target shape and optimal shape, which shows the interaction forces can be reduced while maintaining the shape close to the target shape also for Surface 3 using a limited number of hinge+slot joints,.

Table 14: Norm of error between target shapes and continuous beams of Surface 3.

		All hinge	All hinge+slot	Optimal
Curve A	x-dir.	0.0174	0.0114	0.0184
	y-dir.	0.4493	0.4310	0.4455
	z-dir.	0.0529	0.0459	0.0520
Curve B	x-dir.	0.3892	0.3733	0.3860
	y-dir.	0.2252	0.2158	0.2232
	z-dir.	0.0529	0.0459	0.0520
Curve C	x-dir.	0.3892	0.3733	0.3860
	y-dir.	0.2252	0.2157	0.2234
	z-dir.	0.0529	0.0459	0.0520

7. Static properties of optimal gridshells

In this section, large-deformation analysis against external loads is carried out for verification of static structural properties of the optimal gridshells. Columns and tie bars are connected to the boundary of the structure. All hinge and hinge+slot joints are rigidly connected, because we assume in the practical design that bolts at all joints are fixed after obtaining the desired shape.

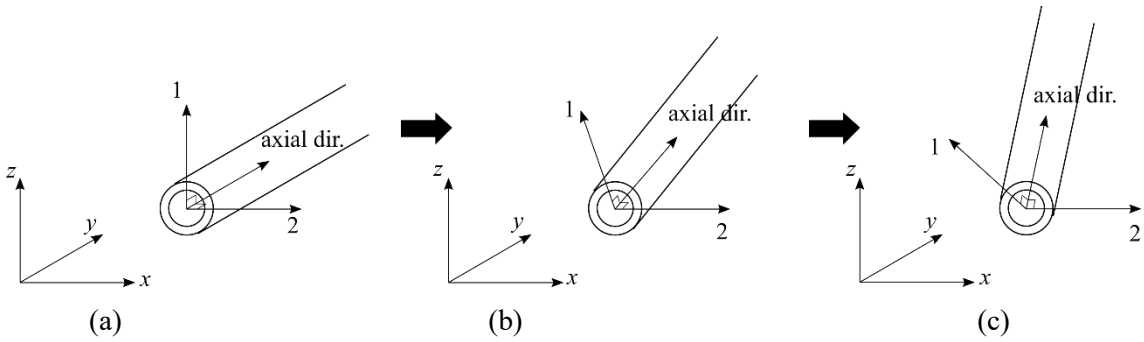

Figure 16: Local coordinates of beam, (a) initial undeformed state, (b) deformed state at self-equilibrium state, (c) final deformed state under static loads.

Figure 16 shows the local coordinates of a beam. The self-equilibrium state in Fig. 16(b) is computed using the deformation obtained in Sec. 6 to define the configuration for analysis against the external loads. Note that the relative displacements at slots are also incorporated. Axis 1 of each beam is in the normal direction of the surface at the self-equilibrium state that is defined by rotation the normal axis from the initial undeformed state on a plane. Since the normal vectors at two ends of each beam are different, the average of those two vectors are taken as the normal vector of a beam. Furthermore, the member axis is redefined by connecting the two nodes of both ends of each member. This process is necessary, because each node is fixed before analysis under

external loads, and the two steps of analysis cannot be done successively. Section forces shown in the following tables are summation of the results of the analysis for generating self-equilibrium shape and the analysis against external loads. The columns and tie bars, respectively, have 0.10 × 0.10 (m) and 0.02 × 0.02 (m) square sections, and their material is steel with Young's modulus 210.0 GPa, Poisson's ratio 0.3, weight density 78.50 kN/m^3, and the yield stress 325 MPa.

Let P_{S}, P_{L}, and P_{H} denote the self-weight, the load representing the weight of roof, and the horizontal load representing seismic load, respectively. The following three types of loading conditions are considered:

Load 1: P_{S}
Load 2: $P_{\mathrm{S}} + P_{\mathrm{L}}$
Load 3: $P_{\mathrm{S}} + P_{\mathrm{L}} + P_{\mathrm{H}}$

where $P_{\mathrm{L}} = 1.0$ kN/m^2 and $P_{\mathrm{H}} = 0.3\left(P_{\mathrm{S}} + P_{L}\right)$ in the following examples. The load P_{L} is applied as concentrated load at each joint proportionally to the covering area. Deformation D_k $\left(k \in \{x, y, z\}\right)$ of each curve of elastica is defined as the mean absolute value of the norm of displacements in global coordinates at the nodes on the elastica as

$$D_k = \sqrt{\frac{1}{n}\sum_{i=1}^{n}\left(u_i^k\right)^2}, \qquad \left(k \in \{x, y, z\}\right) \tag{11}$$

where n is the number of nodes on an elastica and u_i^k is the displacement of the ith node in the direction of kth coordinate. The stress ratio S^{R} is calculated from

$$S^{\mathrm{R}} = \frac{|\sigma_{\mathrm{S}} + \sigma_{\mathrm{L}}|}{\sigma_{\mathrm{y}}} \tag{12}$$

where σ_S and σ_{L} denote the maximum absolute values of stress at the self-equilibrium shape and the stress due to external loads, respectively, and σ_{y} is the yield stress.

Surface 1

Two tie bars and two columns are connected to both ends of Curves B and C, respectively, as shown in Fig. 17. The lower end of each column is fixed at the ground. The horizontal load P_{H}

in Load 3 is applied in the direction of Curve B in the xz-plane. Table 15 shows the norm of deformation derived from Eq. (11). As seen from the table, the self-weight has little effect on the deformation of gridshell, and deformation of Curve B in x-direction has large values about 0.10 m for Load 3. The center nodes of Curves B and C have also large displacements; however, these values are small enough for practical application. Table 16 shows the mean and maximum values of section forces and maximum stress ratios. It is seen from the table that the optimal gridshells are in elastic range for all load cases.

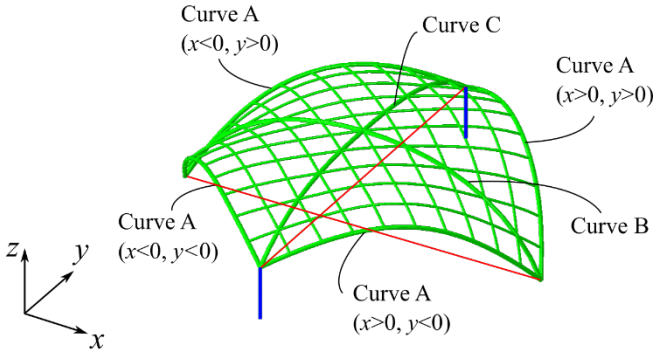

Figure 17: Self-equilibrium shape of Surface 1 composed of continuous beams, tie bars (red lines), and columns (blue lines).

Table 15: Norm of deformation of Surface 1.

		Load 1	Load 2	Load 3	
				$x < 0$	$x > 0$
Curve A $(x < 0, y > 0)$ or $(x > 0, y < 0)$	D_x	0.0006	0.0136	0.0664	0.0873
	D_y	0.0002	0.0052	0.0121	0.0206
	D_z	0.0005	0.0115	0.0486	0.0714
Curve A $(x > 0, y > 0)$ or $(x < 0, y < 0)$	D_x	0.0006	0.0134	0.0666	0.0873
	D_y	0.0002	0.0052	0.0122	0.0206
	D_z	0.0005	0.0117	0.0484	0.0718
Curve B (in xz-plane)	D_x	0.0010	0.0240	0.1071	
	D_y	0.0000	0.0001	0.0001	
	D_z	0.0022	0.0529	0.0579	
Curve C (in yz-plane)	D_x	0.0000	0.0001	0.0752	
	D_y	0.0003	0.0070	0.0068	
	D_z	0.0022	0.0526	0.0519	

Table 16: Mean and maximum values of section forces and maximum stress ratio of Surface 1.

		Load 1	Load 2	Load 3
Mean section force [kN]	Axial force	13.400	12.499	14.374
	Shear force in 1-dir.	2.9767	2.7815	3.0436
	Shear force in 2-dir.	1.4547	1.3667	1.9238
Maximum section force [kN]	Axial force	50.097	36.593	45.275
	Shear force in 1-dir.	12.360	13.033	16.395
	Shear force in 2-dir.	19.363	19.586	20.689
Maximum stress ratio		0.09502	0.10992	0.13897

Surface 2:

Figure 18 shows the self-equilibrium shape of Surface 2. Seven columns with height 3 m are connected to the internal connections, and the tie bars exist between both ends of curved beam and the bottom of column. Displacements in x- and z-directions and rotation around y-axis are fixed at the both ends of seven beams. The horizontal load P_{H} in Load 3 is applied in y-direction along the primary beams. It is seen from Table 17 that self-weight has little effect on deformation of the gridshell, and deformation of Curve D in z-direction has large values about 0.07 m for Load 3. Deformation of the outer curves in z-direction is larger than the inner curves for Loads 1 and 3. The maximum stress ratios in Table 18 verify that the optimal gridshells are in elastic range for all load cases.

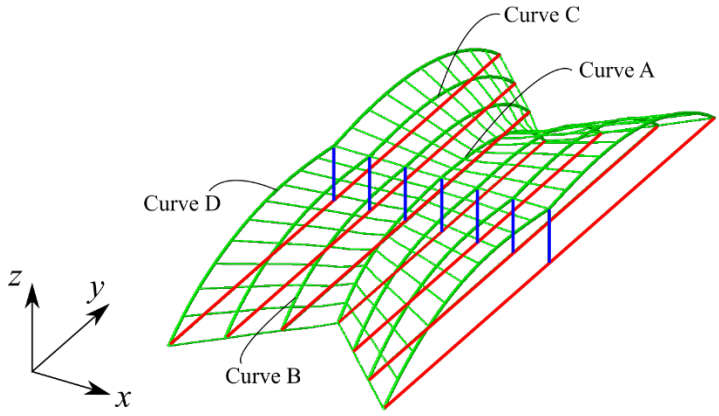

Figure 18: Self-equilibrium shape of Surface 2 composed of continuous beams, tie bars (red lines), and columns (blue lines).

Table 17: Norm of deformation of Surface 2.

		Load 1	Load 2	Load 3
Curve A ($x = 0$)	D_x	0.0001	0.0001	0.0001
	D_y	0.0002	0.0054	0.0252
	D_z	0.0007	0.0240	0.0362
Curve B ($x = \pm 2$)	D_x	0.0010	0.0022	0.0032
	D_y	0.0015	0.0070	0.0287
	D_z	0.0010	0.0311	0.0464
Curve C ($x = \pm 4$)	D_x	0.0021	0.0028	0.0058
	D_y	0.0014	0.0088	0.0335
	D_z	0.0024	0.0405	0.0585
Curve D ($x = \pm 6$)	D_x	0.0012	0.0034	0.0053
	D_y	0.0016	0.0093	0.0318
	D_z	0.0019	0.0350	0.0558

Table 18: Mean and maximum values of section forces and maximum stress ratio of Surface 2.

		Load 1	Load 2	Load 3
Mean section force [kN]	Axial force	18.602	27.404	27.361
	Shear force in 1-dir.	0.5027	0.5544	0.5877
	Shear force in 2-dir.	2.2441	2.4196	2.4783
Maximum section force [kN]	Axial force	78.550	101.48	105.44
	Shear force in 1-dir.	4.7340	5.4945	6.1260
	Shear force in 2-dir.	24.024	28.685	33.455
Maximum stress ratio		0.38451	0.38453	0.38420

Surface 3:

Three tie bars are connected to both ends of Curves A, B and C. Displacements at all ends of the primary beams are fixed in x-, y- and z-directions. We apply horizontal load P_{H} in x- and y-directions separately for Load 3, i.e. there are two load cases in Load 3. As seen from the the norm of deformation in Table 19, self-weight has little effect on the deformation of gridshell, and deformation of Curve A in x-direction, and Curves B and C in y-direction have large values about 0.05 m for Load 3. It is also seen from the maximum stress ratios in Table 20 that the optimal gridshells are in elastic range for all load cases.

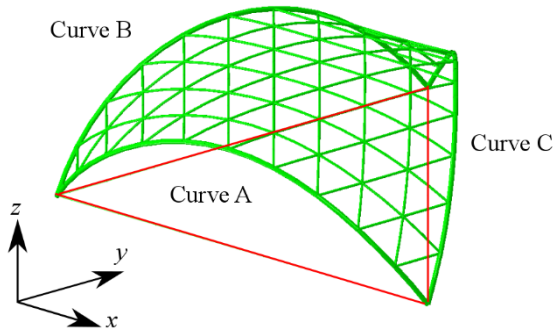

Figure 19: Self-equilibrium shape of Surface 3 composed of continuous beams and tie bars (red lines).

Table 19: Norm of deformation of Surface 3.

		Load 1	Load 2	Load 3 (x-dir.)	Load 3 (y-dir.)
Curve A	D_x	0.0005	0.0090	0.0538	0.0082
	D_y	0.0003	0.0054	0.0098	0.0368
	D_z	0.0007	0.0127	0.0406	0.0114
Curve B	D_x	0.0003	0.0062	0.0418	0.0028
	D_y	0.0004	0.0083	0.0128	0.0527
	D_z	0.0007	0.0126	0.0223	0.0372
Curve C	D_x	0.0004	0.0071	0.0498	0.0024
	D_y	0.0004	0.0083	0.0073	0.0524
	D_z	0.0007	0.0127	0.0276	0.0369

Table 20: Mean and maximum values of section forces and maximum stress ratio of Surface 3.

		Load 1	Load 2	Load 3 (x-dir.)	Load 3 (y-dir.)
Mean section force [kN]	Axial force	11.612	11.386	11.669	11.639
	Shear force in 1-dir.	1.3023	1.3067	1.3085	1.3090
	Shear force in 2-dir.	2.2256	2.1769	2.2106	2.2109
Maximum section force [kN]	Axial force	37.986	44.063	53.670	52.136
	Shear force in 1-dir.	19.010	19.656	20.457	20.479
	Shear force in 2-dir.	10.107	12.974	16.878	16.572
Maximum stress ratio		0.18252	0.16828	0.17257	0.17056

8. Conclusions

We presented a method for designing gridshells using discrete elastica, which consists of rigid bars connected with rotational springs. The stiffness of each rotational spring is derived from the equivalence of the strain energy between the discrete and continuous elastica models. The shape of discrete elastica is found by solving an optimization problem for minimizing the total potential energy consisting of discretized form of penalized strain energy and the external work corresponding to the external moments. By solving the problem under constraints on the span length and the height of supports, we can generate various shapes of discrete elastica. Furthermore, the reaction forces needed for deformation can be found from the Lagrange multipliers.

Target shape of a curved surface of gridshell is specified by connecting several discrete elasticas as primary beams, which are connected with thin secondary beams. It has been confirmed by large-deformation analysis that the surface shape obtained by assigning forced displacements and external moments is close to the target shape defined using the discrete elastica. Therefore, we can expect that the interaction forces at the joints are very small, because the elastica is a self-equilibrium shape under bending deformation.

The hinge joints can be replaced by hinge+slot joints to further reduce the interaction forces at joints on the gridshell surface. A combinatorial optimization method has been proposed to find the optimal locations of the specified number of hinge+slot joints. We solved this problem using SA, and confirmed that the maximum interaction forces are drastically reduced by assigning several hinge+slot joints.

It has also been confirmed that the deformation of optimal gridshell is small enough under gravity and static horizontal loads. Therefore, the proposed optimization method using discrete elastica and hinge+slot joints may be a practical tool for design of bending-active gridshells.

Appendix

Simulated annealing (SA):

SA is one of the metaheuristic approaches to combinatorial optimization problems. SA searches wide range of feasible region by allowing transition to a worse solution within a given probability. The algorithm for minimizing the objective function $\Pi(\boldsymbol{x})$ of variables $\boldsymbol{x} = (x_1, \ldots, x_n)$ is summarized as [18,19]:

Step 1: Set the iteration counter $k = 0$. Assign the initial solution $\boldsymbol{x}_k$ randomly, and evaluate the value of $\Pi(\boldsymbol{x}_k)$. Assign the initial temperature parameter as $T_k = 1.0$.

Step 2: Randomly generate neighborhood solutions, and find the best solution $\boldsymbol{x}^*$ that minimizes the objective function.

Step 3: If $\Pi(\boldsymbol{x}^*) < \Pi(\boldsymbol{x}_k)$, then accept $\boldsymbol{x}^*$ as $\boldsymbol{x}_{k+1} = \boldsymbol{x}^*$; otherwise, accept $\boldsymbol{x}^*$ with the following probability:

$$P = \exp\left(\frac{\Pi(\mathbf{x}_k) - \Pi(\mathbf{x}^*)}{\alpha T_k}\right)$$

where α is the scaling factor.

Step 4: Update the temperature as $T_{k+1} = \eta T_k$, where η is a parameter in the range $0 < \eta < 1$.

Step 5: If termination condition is not satisfied, let $k + 1 \leftarrow k$ and go to Step 2; otherwise, output the best solution and terminate the process.

Acknowledgement

This study is partially supported by JSPS KAKENHI No. 16K14338.

References

[1] Adriaenssens S, Block P, Veenendaal D, Williams C (Eds.). Shell Structures in Architecture: Routledge, London; 2014.

[2] Tayeb F, Lefebre B, Baverel O, Caron JF, Du Peloux L. Design and realization of composite gridshell structures. J Int Assoc Shell and Spatial Struct 2015;56:49-59.

[3] Douthe C, Caron JF, Baverel O. Form-finding of a gridshell in composite materials. J Int Assoc Shell and Spatial Struct 2006;47:53-62.

[4] Bouhaya L, Baverel O, Caron JF. Optimization of gridshell bar orientation using a simplified genetic approach. Struct Multidisc Optim 2014;50:839-848.

[5] Barnes MR. Form-finding and analysis of prestressed nets and membranes. Comp Struct 1988;30(3):685-695.

[6] Adriaenssens S, Barnes MR. Tensegrity spline beam and grid shell structures, Eng Struct 2001;23:29-36.

[7] Linkwitz K, Schek HJ. Einige Bemerkungen zur Berechnung von vorgespannten Seilnetzkonstruktionen. Ingenieur-Archin 1971:40:145-158.

[8] Schek HJ. The force density method for form finding and computation of general networks. Comput Methods Appl Mech Eng 1974:3:115-134.

[9] Jensen TJ, Baverel O, Douthe C. Morphological and mechanical investigation of interconnected gridshells. Int J Space Struct 2013;28(3-4):175-186.

[10] Kuijvenhoven M, Hoogenboom PCJ. Particle-spring method for form finding grid shell structures consisting of flexible members. J Int Assoc Shell and Spatial Struct 2011;53(1):31-38.

[11] Ohsaki M, Seki K, Miyazu Y. Optimization of locations of slot connections of gridshells modeled using elastica. Proc IASS Symposium 2016, Tokyo. Int Assoc Shell and Spatial Struct 2016;Paper No. CS5A-1012, www.iass-structures.org/index.cfm/proceedings.index.

[12] Matsuo A, Ohsaki M, Miyazu Y. Optimization of elastically deformed gridshell with partially released joints. Proc IASS Working Group 12+18 Int Colloquium 2015. Int Assoc Shell and Spatial Struct 2015;Paper No. 15T-03.

[13] Brunnett G, Wendt J. A univariate method for plane elastic curves. Comput-Aided Geom Des 1997;14:273-292.

[14] Levyakov SV, Kuznetsov VV. Stability analysis of planar equilibrium configurations of elastic rods subjected to end loads. ACTA Mech 2010;211:73-87.

[15] Bessini J, Lázaro C, Monleón S. A form-finding method based on the geometrically exact rod model for bending-active structures. Eng Struct 2017;152:549-558.

[16] Watson LT, Wang CY. A homotopy method applied to elastica problems. Int J Solids Struct 1980;17:29-37.

[17] Bruckstein AM, Holt RJ, Netravlai AN. Discrete elastica. Appl Anal 2010;78:453-485.

[18] Chalamel N, Kocsis A, Wang CM. Discrete and non-local elastica. Int J Non-Linear Mech 2015;77:128-140.

[19] Aarts E, Korst J. Simulated Annealing and Boltzmann Machines: A Stochastic Approach to Combinatorial Optimization and Neural Computing. Wiley, New York; 1989.

[20] Ohsaki M. Optimization of Finite Dimensional Structures. CRC Press, Boca Raton, FL; 2011:.

[21] Kirkpatrick S, Gelatt CD, Vecchi MP. Optimization by simulated annealing. Science 1983;220:671-680.

[22] Djondjorov PA, Hadzhilazova MTS, Mladenov IM, Vassilev VM. Explicit parametrization of Euler's elastica. Proc 9th Int Conf on Geometry, Integrability and Quantization, Bulgaria 2008;175-186.

[23] Gill PE, Murray W, Saunders MA. SNOPT: An SQP algorithm for large-scale constrained optimization. SIAM J Opt 2002;12:979-1006.

[24] Dassault Systèmes. Abaqus User's Manual Ver. 6.16. 2016.

[25] Design standard for steel structures – Based on allowable stress concept, Architectural Institute of Japan, Maruzen, 2015, (in Japanese); English version available online, https://www.aij.or.jp/eng/publish/ index_ddonly.htm.